THE JOURNAL OF PHYSICAL CHEMISTRY C

Article

Cite This: J. Phys. Chem. C 2019, 123, 11310−11318

pubs.acs.org/JPCC

Connecting Theory with Experiment to Understand the Sintering Processes of Ag Nanoparticles

Edison Z. da Silva,*[,†] Giovani M. Faccin,[‡] Thales R. Machado,[§] Nadia G. Macedo,[§] Marcelo de Assis,[§] Santiago Maya-Johnson,[§] Júlio C. Sczancoski,[§] Juan Andrés,[∥] Elson Longo,[§] and Miguel A. San-Miguel[⊥]

[†]Institute of Physics "Gleb Wataghin", UNICAMP, CP 6165, 13083-9859 Campinas, SP, Brazil

[‡]Faculdade de Ciências Exatas e Tecnológicas, Universidade Federal da Grande Dourados—Unidade II, CP 533, 79804-970 Dourados, MS, Brazil

[§]CDMF, LIEC, Federal University of São Carlos (UFSCar), P.O. Box 676, 13565-905 São Carlos, SP, Brazil

[∥]Department of Analytical and Physical Chemistry, University Jaume I (UJI), Castelló 12071, Spain

[⊥]Instituto de Química, UNICAMP, CP 6165, 13083-970 Campinas, SP, Brazil

Supporting Information

ABSTRACT: A complementary combination of long-time atomistic molecular dynamics simulations and real-time transmission electron microscopy (TEM) images has been utilized for unraveling, at an atomic resolution, the nature of the sintering process of Ag nanoparticles (NPs) induced on the surface of an α-Ag_2WO_4 crystal for the first time, under the exposure of a TEM electron beam (EB). Temporal evolution of calculated and experimental results highlights the role of the lattice plane matching and the stacking faults along the disorder-to-order transitions of the oriented attachment process. This phenomenon is considered as an example of surface plasmon resonances (SPRs), in which the EB has two effects: first, it provokes the formation of the Ag NPs that, due to the electron irradiation, become SPR electric dipoles, and, second, these Ag NPs undergo sintering processes that are controlled by dipole−dipole interactions forming larger clusters. The predictive power of the simulation model was verified experimentally, paving the way for quantitative predictions of the events involved in the Ag NP sintering process. These findings reveal the atomic-scale dynamics, which helps advance the general understanding and provides further support and reliability of the conclusions of this study.

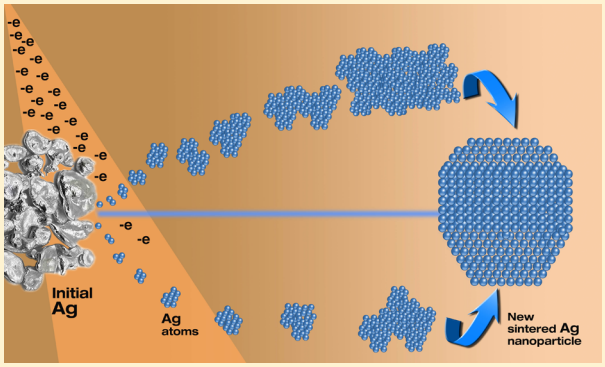

INTRODUCTION

Transmission electron microscopy (TEM) is a well-established technique for characterization on a nano and an angstrom scale, in which high-energy electrons transmit through the specimen. The analysis of energy exchanges between the electrons and the sample adds further information regarding the chemical composition and electronic structure of the samples based on electron−solid interactions, which is of significance for both fundamental research and potential technological applications.[1−4] There is much evidence of the formation and growth of Ag nanoparticles (NPs) within the area irradiated by the electron beam (EB) on different Ag-based micro/nanostructures.[1,5−11] These syntheses, which employ the EB of the TEM, are particularly valuable because the microscopes enable one to elucidate the nanoscale structural evolution of the Ag NPs as they are being synthesized. Five years ago, our group started a research line based on the observation of the formation of Ag NPs on different Ag-containing compounds (α-Ag_2WO_4,[12−15] β-Ag_2WO_4,[16,17] β-Ag_2MoO_4,[18] Ag_2CrO_4,[19] β-$AgVO_3$,[20] and Ag_3PO_4[21]) induced by the irradiation of an EB from TEM in vacuum. These works facilitated a series of experimental and theoretical studies to reach interesting possibilities of producing Ag NPs on these materials because the synergism between the support semiconductor and Ag NPs can enhance their stability and the corresponding performance in promising technological applications like photoluminescence and bactericide materials.[22−24] In this context, the recent review by Zhang et al.[25] highlights the progress in the synthesis of Ag NPs and the formulation of sintered Ag paste with enhanced mechanical, electrical, and thermal conductivity properties.

The sintering process governs the initial stage of the junction of the grain boundaries in which two initially isolated particles

Received: March 5, 2019
Revised: April 11, 2019
Published: April 11, 2019

DOI: 10.1021/acs.jpcc.9b02107
J. Phys. Chem. C 2019, 123, 11310−11318

bond together to form larger particles. This is an activated process, and it plays a prominent role in controlling several properties of the resulting particle, such as the particle size and the particle size distribution. Sintering of metal NPs has been investigated in the past decade both experimentally[12,13,26−31] and computationally.[29,32−36] These processes involve at least three stages: the approach between NPs, the oriented attachment (OA) involving prealigned crystallographic orientations or the imperfect oriented attachment (IOA) when touching occurs with different surface planes and angles, and the subsequent coalescence or aggregation process to form a single NP. The understanding of nanoparticle sintering is, therefore, essential for obtaining nanoparticles or nanocrystalline materials with desired physical and chemical properties. Detailed knowledge on these stages along the sintering process and the interaction between active NPs is, thus, of considerable importance, but it still poses a significant challenge.[37,38] Molecular dynamics (MD) simulation represents a powerful tool to provide detailed insights into the molecular mechanisms that drive and control the interactions between NPs. By solving the equation of motion for a large system of particles, the real behavior of materials at a specified temperature can be simulated. The trajectory and physical movement of NPs in the system can also be determined and analyzed. Recently, MD simulations have been successfully used to investigate the sintering process of different metals (Al, Cu, and Ni)[36,39,40] and metal oxides (TiO_2[41] and CuO[42]).

Surface plasmon resonance (SPR) effects appear in metal NPs, and they are associated with the frequencies of collective oscillations of the free electrons that fall in the optical range of the electromagnetic spectrum.[43,44] Plasmonic metal NPs can concentrate incident optical fields in nanometer-sized volumes. This leads high local fields to not only enhance optical responses but also induce chemical transformation, driven by plasmon-induced hot carriers (optical spectroscopies).[45] Actually, plasmons were first revealed as energy loss features in the spectra of electrons rejected from metal surfaces.[46] Since then, EBs have become an important tool to yield information on plasmons.[47−49] Light could be used as the energy source in the synthesis of Ag NPs[50,51] and Au NPs.[52,53] Previous studies of metal NPs have shown that, similar to the case of laser irradiation, EB irradiation produces electromagnetic wave radiation (EWR) that acts on the NPs producing SPR nanodipoles. In this process, Ag NPs are wavelength (or frequency) filters capable of absorbing EWR in specific frequencies, which excites SPR on the Ag NPs.[54−56] Therefore, nearby Ag NPs in bonding states attract each other, and this is the driving effect to start the sintering process.

EXPERIMENTAL SECTION

The initial precursors comprising α-Ag_2WO_4 nanorods were synthesized by chemical precipitation in dimethyl sulfoxide, in accordance with the methodology described by Sczancoski et al.[57] For the in situ TEM experiments, the resulting α-Ag_2WO_4 powder was redispersed in water by sonicating for 5 min and then one drop of the dispersion was applied to a 300 mesh Cu grid coated with an ultrathin carbon support. The TEM experiments were carried out using a TITAN Themis Cubed double-corrected microscope (ThermoFisher Scientific) equipped with a gun monochromator and extreme field emission gun (X-FEG), a high-brightness emitter gun operating at 300 kV. The microscope is located in the facilities of the Brazilian Nanotechnology National Laboratory (LNNano) in the National Center of Research in Energy and Materials (CNPEM). For the growth of mother Ag particles, the entire α-Ag_2WO_4 nanorod was illuminated for a few minutes by the electron beam generated during TEM operation. This step causes the extrusion and reduction of Ag species from the crystalline lattice of the precursor oxide and the subsequent crystallization of Ag particles at the surface of the α-Ag_2WO_4 nanorods. A gradually converging electron beam was used to illuminate the mother Ag particles necessary to promote an explosive reaction where many Ag NPs are fragmented. These NPs are then caught by the carbon film of the TEM grid. A continuous irradiation of these segregated NPs for a long exposure time (0−253 s) was used to promote the dynamic bonding events. The high-resolution transmission electron microscopy (HRTEM) experiments were carried out using a spot size 4 and a dose rate of approximately 6×10^5 A/m^2 ($\approx 3.6 \times 10^6$ e/nm^{2}s).

THEORY

Molecular dynamics simulations were performed using the LAMMPS package[58−61] and the embedded atom model,[62−65] with the parameterization for Ag from Sheng et al.,[66] which was recently used to study Ag NPs under similar conditions.[67−70] Wulff-shaped NPs were modeled after the experimental measurements, thus resulting in NP models of similar size and exposed facets, in particular, (111) and (220) ones. Figure S1 in the Supporting Information (SI) material shows two views of the models. Details of the preparation are described in the SI. After relaxing the models, a thermal study of their behavior prior to sintering was performed and is presented in the SI. The sintering process was studied by approaching the two NPs in a set of simulations using canonical ensemble molecular dynamics with Nosé−Hoover thermostat chains[71−73] at 700 K. Visualizations were created using the visual molecular dynamics (VMD) and Ovito packages[74−76] and the common neighbor analysis (CNA) of Honeycutt et al.[77] that discriminates the local structure of each atom, with the color coding where green atoms are in an face-centered-cubic (fcc) structure, red atoms are in an hexagonal close-packed (hcp) structure, and gray atoms are in a disordered structure. The results are shown in Figure 3.

RESULTS AND DISCUSSION

Kinetics of NP Sintering. The kinetics of NP sintering is governed by processes on two quite different length scales. The longer length scale involves the diffusive transport of heat, while the intrinsic growth rate, in contrast, is governed by the nanoscopic dynamics associated with the cooperative reorganization at the NP interface. In this study, direct atomic resolution was conducted to explore the fundamental understanding of the sintering mechanism of Ag NPs formed on the α-Ag_2WO_4 material under EB irradiation. The novelty of this work is related to the fact that essential information was collected at an atomic level, from real in situ TEM images and MD simulations, to study the interactions between the Ag NPs that, under the EWR, developed into SPR resonances (nanoelectrical dipoles), and then the nature of the sintering mechanism was disclosed. These are necessary for studying structural evolution, changing growth regimes, and providing insights into the sintering process. The study started with the exploration of the trajectories of Ag NPs by observing the coalescence events of the different Ag NPs. Most of the time,

DOI: 10.1021/acs.jpcc.9b02107
J. Phys. Chem. C 2019, 123, 11310−11318

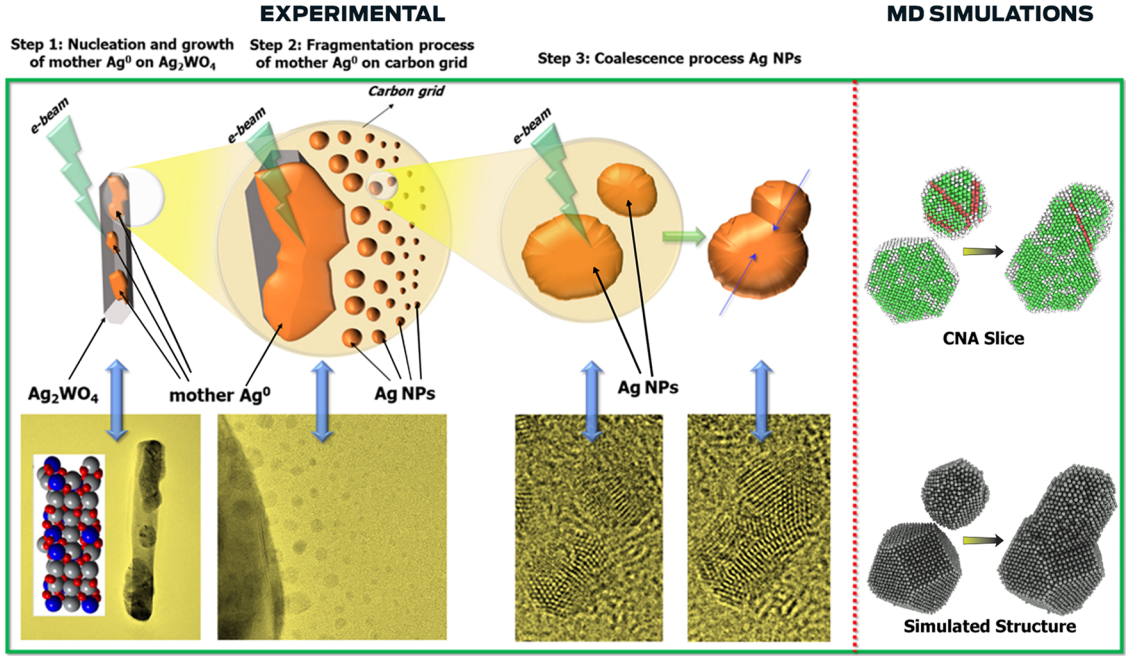

Figure 1. Schematic representation of experimental and theoretical results of the present study. The sintering process starts with the nucleation and growth of mother Ag^0 particles on α-Ag_2WO_4 (step 1). The exposure of the EB from TEM induces the reduction of the Ag cations, which migrate from the α-Ag_2WO_4 bulk crystal structure to form mother Ag^0 on the α-Ag_2WO_4 surface. When the EB is focused on these mother Ag^0, a fragmentation process takes place in which smaller Ag NPs become free on the carbon grid (step 2). These free Ag NPs are involved in the aggregation or coalescence processes (step 3). To understand the last step further, MD simulations were performed.

Ag NPs keep moving randomly, but sometimes, they are found along the viewing zone axis, and, despite occasional off-axis fluctuations, it is possible to identify their orientations by lattice fringes. Understanding the analogies between the experimental and simulated scenarios implies new strategies for rational comprehension of the sintering process. Based on this knowledge, the following four questions will be answered. How is the formation of Ag NPs, in the range from 4 to 8 nm, induced by EB irradiation on α-Ag_2WO_4 crystals in vacuum? What physical parameters determine the rate of Ag NP aggregation? What is the role of the stacking faults along the disorder-to-order transitions of the sintering process? What is the physical origin responsible for the sintering process of Ag NPs provoked by the interaction between matter and EBs?

Real-Time Sintering of Ag NPs. A schematic representation of the studied phenomena by joint use of experimental and theoretical methods is depicted in Figure 1. The EB of TEM provokes the segregation of the metal Ag^0 atoms from the bulk to the surface of the α-Ag_2WO_4 crystal, with concomitant formation and growth of Ag NPs, called "mother Ag^0 particles," on top of the surface. As reported in previous studies with α-Ag_2WO_4, as soon as the EB hits the semiconductor sample, the Ag nucleation process begins (step 1).[12,13,22,23] This nucleation process is the result of the action of the electrons from the beam, which are transferred to the material from one cluster to another through the lattice network. The Ag nucleation is a consequence of the reduction of the Ag^+ in different extents of the $[AgO_x]$ (x = 2; 4; 6; 7) clusters into Ag^0, which promotes a transformation from an ordered structure of α-Ag_2WO_4 to a disordered one. The growth of Ag NPs on α-Ag_2WO_4 is a consequence of structural order/disorder effects generated on the semiconductor material when the EB passes through it.[14,26] This phenomenon is similar to the grain boundary migration-dominated pathway proposed by Li et al. to explain the crystal nucleation and growth initiated from an amorphous state of Bi metal under an EB inside an aberration-corrected TEM.[78] Once Ag NP nucleation and growth happen in step 1, the incoming electrons promote new phenomena on the studied system.[14] Thus, not only can the formation of Ag NPs on the surface of α-Ag_2WO_4 at initial instants be observed, but also the continued exposure to the EB can lead to a fragmentation process of the as-formed Ag NPs and subsequent appearance of free Ag NPs in vacuum (step 2).[14] This phenomenon is a consequence of the increasing exposure of the large initial Ag NPs to the EB, which makes them unstable, experiencing several structural changes, until the occurrence of an explosive reaction, with the ejection outward of a large number of Ag NPs.[1] This is a well-known process that results from the transfer of thermal energy and electric charge[79] and takes place in metallic samples, which can melt and collapse into units as the irradiating current density increases. The newly formed Ag NPs can be expelled and "fly" in the carbon grid for some nanometers of distance, as observed. These Ag NPs become electric dipoles, and they are the building blocks to start the coalescence process (step 3), as shown in Figure 1. The sizes of the Ag NPs are in the range from 4 to 8 nm, and their aggregation or coalescence process occurs through motion of the Ag NPs driven by the electron forces, ending in a mass transfer process that produces larger and well-defined Ag NPs, with more stable configurations.[14,80] A video of the coalescence step is available in the SI section (Video S1).

The experiments show the temporal evolution of the free-flying Ag NPs and their interactions, forming other larger Ag NPs. These processes can be understood from Mie theory, as an example of SPR effects, in which neutral dipole interactions are used to explain them. The interaction among the Ag NPs comprises three different types: orientation and induction,

DOI: 10.1021/acs.jpcc.9b02107
J. Phys. Chem. C 2019, 123, 11310−11318

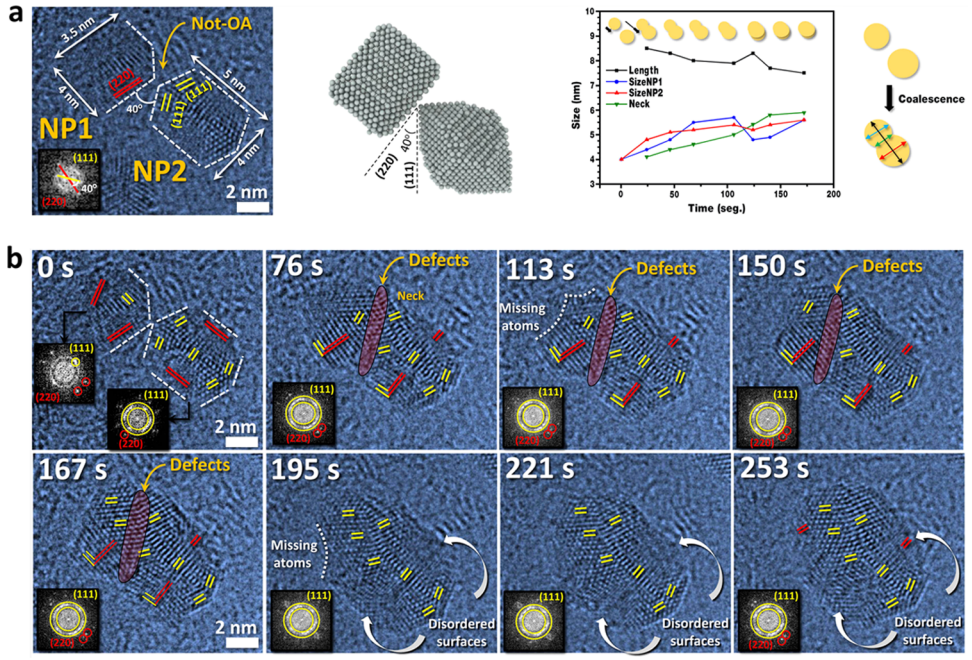

Figure 2. Sintering events of the Ag NPs. (a) High-resolution transmission electron microscopy (HRTEM) images of two Ag NPs, NP1 and NP2 (left). Both Ag NPs are multifaceted, and the main exposed planes, (220) and (111), are displayed in this image. The fast Fourier transform (FFT), at the inset, shows the crystallographic planes near the contact region of these Ag NPs, evidencing an initially disorder-driven event by the estimation of angle between the (220) and (111) planes (red and yellow lines, respectively). These Ag NPs were simulated, and the results are presented at the center of the figure. Estimations of the particle and neck sizes with distinct exposure times to the EB are given (right). (b) Sequence of HRTEM images evidencing the coalescence process of the Ag NPs under the EB exposure. The FFTs (insets) obtained from these Ag NPs show the main crystallographic planes, (220) and (111), illustrated as red and yellow lines, respectively.

which can be explained by the classical theory, and dispersion, which can only be rationalized by the quantum mechanics. The orientation interaction results from the correlation between the rotational motions of the permanent moments of the Ag NPs, while the induction interaction is caused by the polarization of the Ag NP by the permanent moment of another Ag NP. The dispersion interaction arises from the correlation of the motions of electrons in neighboring clusters.[81,82] Because the Ag NPs under the EB become SPR nanodipoles with Ag NPs of sizes ranging from 4 to 8 nm, these nearby Ag NPs interact via dipole−dipole interactions, and this leads to the formation of dimers that come in contact to start a coalescence process, forming new Ag NPs, as was observed in the present experiments. Therefore, it is believed that these events are clear evidence of the mechanism described here. The Ag NPs interact with different surface planes; therefore, the coalescence process discussed in this work does not involve crystalline-oriented attachment, for reasons that will be discussed further.[83] The mechanism underlying this unusual in situ Ag NP formation requires careful examination on a physical basis. To this end, and as a valuable complement to such experimental observations, a comprehensive study was carried out using MD simulation methods, and it provides insights into the structural changes and energetic properties of the Ag NPs, to unveil the details of the coalescence process to complement the experimental findings.

Figure 2 shows the experimental results obtained for two well-defined Wulff-shaped Ag NPs, NP1 and NP2, with different exposed facets. In each surface, distinct planes can be indexed, mainly related to (220) and (111), in accordance with the JCPDS database (PDF-04-0783) for face-centered-cubic (fcc) metallic Ag^0 structures. Initially, at time 0 s (Figure 2a, left), just after the fragmentation process of the mother Ag NP, the newly formed Ag NPs are separated by 0.4 nm at the closest distance of the point between the (220) surface of NP1 and the corner formed by (111) facets of NP2. The angle between these crystallographic planes was measured to be 40° by identifying their Fourier reflections (inset). Hence, the distinct planes that are exposed at these surfaces, as well as their misalignment, lead to an initially disorder-driven process. The dimensions of these Ag NPs are quite similar: 3.5 nm × 4.0 nm (NP1) and 4.0 nm × 5.0 nm (NP2). Figure 2a (center) illustrates the Ag NPs used in the simulations; it shows their contact angles, where a good agreement between the experiments and theoretical simulations is observed. The exposure of the Ag NPs to the EB leads to the coalescence process, and longer exposure times also give energy to the formation and growth of the neck for the sintered Ag NPs. Figure 2a (right) shows the evolution of the Ag NPs and neck sizes as a function of exposure time.

To clarify these events at the atomic level, the effect on the Ag NPs was monitored at distinct exposure times by time-resolved electron microscopy from 0 to 253 s, and Figure 2b shows the obtained results. In these images, one can find different phenomena with high spatial resolution occurring during the welding processes: rotation of Ag NPs to minimize the crystallographic mismatch, growth of the neck between the two Ag NPs, atomic diffusion mainly from facets with exposed (220) planes, ordered/disordered transition of these facets, and formation/healing of the disordered interface. To understand these events, we emphasize the principal crystallographic planes that reorganize during the coalescence process both in real images and by fast Fourier transform (FFT), as well as the observed defects. The FFT of the initial NPs (0 s)

DOI: 10.1021/acs.jpcc.9b02107
J. Phys. Chem. C 2019, 123, 11310−11318

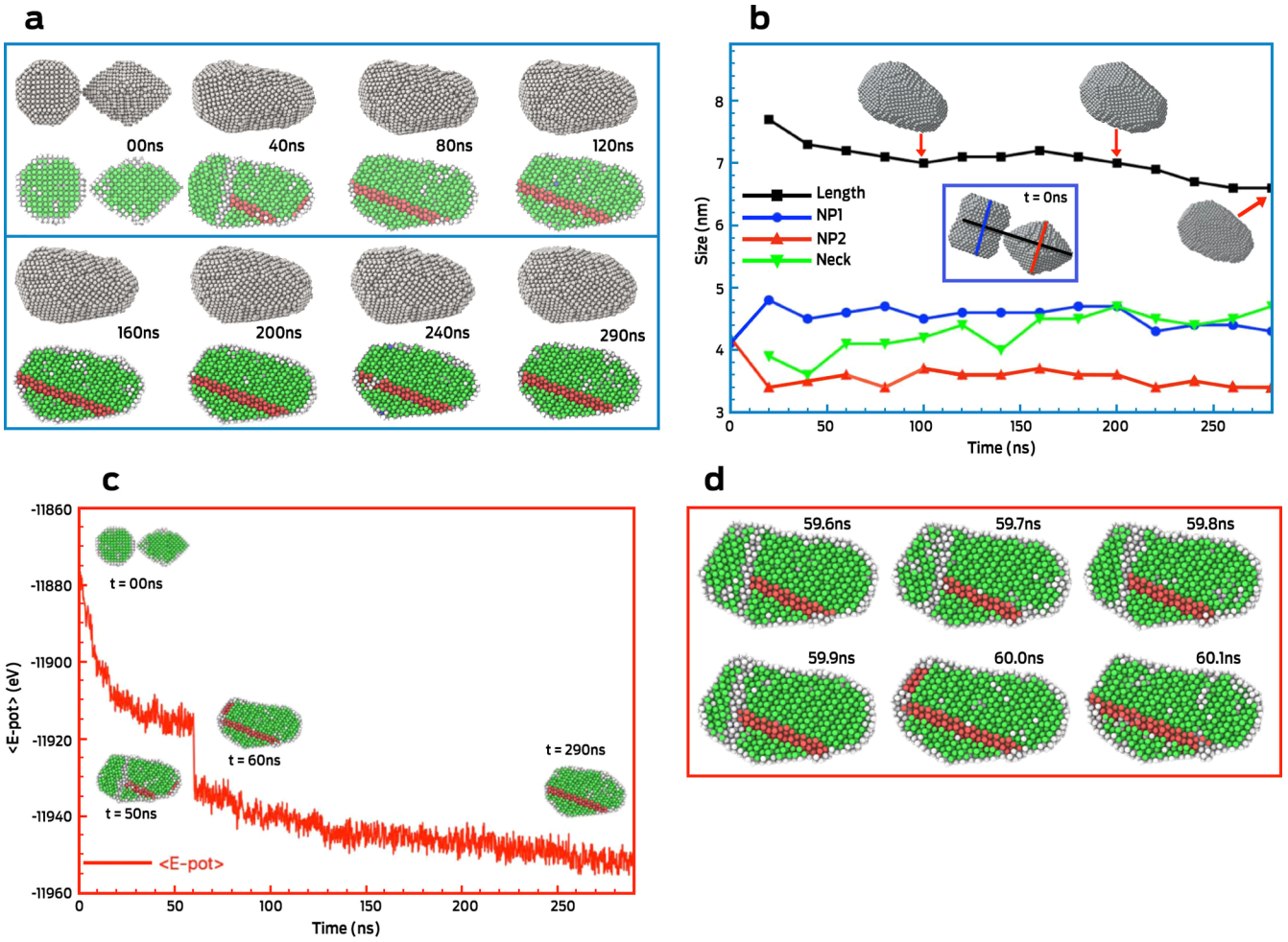

Figure 3. MD simulation of two attached Ag NPs: (a) structures and CNA slice images at different times (green, fcc structure; red, hcp structure; and grey, disordered structure). (b) Evolution of characteristic lengths associated with the process, the length of NP (black line), lateral length of NP1 (blue line), and NP2 (red line), and size of the interface neck (green line). Inset: NP1 and NP2 prior to contact. (c) Average potential energy. CNA insets show initial and final structures as well as the two images associated with the disorder-to-order transition. (d) Detailed time evolution of the process for the disorder-to-order transition.

and the posteriorly formed dimer consists of the typical ones from faceted NPs. Hence, a partial halo (yellow circles in the insets) with specific reflections is observed, and it departs mainly from the (111) plane at distinct facets as well as from the (200) planes (not shown). Other reflections outside this region (red circles in the insets) are observed mainly from (220) planes. The reflections in FFT match well with the crystallographic planes demonstrated in the real images. Considering all of these observations, it can be assumed that the coalescence process of the Ag NPs in the present work is accompanied by neck growth formed between the Ag NPs because of diffusion of surface atoms and not by a simple rigid-body collision.

Initially, at time 0 s, an important mismatch is observed between the (220) and (111) planes from both Ag NPs, which greatly decreases after 76 s, probably as a result of a rotation of Ag NPs. However, the lattice alignment between the Ag NPs remains imperfect, and line dislocations (brown region labeled as defects) are created as an effect of crystal−crystal incoherent bonding, leading to a defect-mediated coalescence of the Ag NPs. Hence, the Ag NPs reorient to a limited extent, and the resulting configuration allows the formation of defects, resulting in misoriented attachment. These defects formed during bonding persist for many seconds until 167 s, where a sudden ordering is observed. During this healing process of the interface, the neck growth and diffusion of mobile Ag atoms (labeled as missing atoms) mainly depart from facets with (220) exposed planes. At the final stage of the coalescence process from 167 to 253 s, three main effects occur: (i) continuous growth of the neck and decrease of facets shared; (ii) increase of crystalline coherency between (111) exposed planes of both Ag NPs, leading to a close-to-oriented bonding; and (iii) disordering of facets, probably because of a high mobility of the Ag atoms in these facets (labeled as disordered surfaces). Moreover, the two FFT spots corresponding to these facets alternate from defined to various diffuse spots, depending on irradiation time between 167 and 253 s. These findings could be associated with a melted state of these less stable surfaces as an effect of the interaction with the high-energy EB. Hence, these atoms could be the major contributors for increased ordering, neck size, and crystalline coherency of the final sintered Ag NP.

Connection to Theory: Coalescence Simulations. The aim here is to understand, at a fundamental level, the nanoscopic processes underlying the experimental data discussed above. The sintering process of two Ag NPs involves

DOI: 10.1021/acs.jpcc.9b02107
J. Phys. Chem. C 2019, 123, 11310−11318

many competing effects, such as surface diffusion caused by preferential melting of high-energy surface atoms and internal competition between the formed disordered/ordered interfaces, preventing healing and, thus, perfect welding. The present MD simulations provide a careful study of how two Ag NPs are capable of forming a larger one, similar to those observed in the experiments (see Figures S1−S5 in the SI for details).

The main idea that explains the interaction between Ag NPs has been discussed previously[34] and can be explained with the help of Mie theory. As shown by Koh et al.,[54] metal Ag NPs in the presence of the EB become SPR objects. This occurs because Ag NPs are wavelength (or frequency) filters for this EWR and the resonance results in SPR-neutral objects.[54−56,84] These SPRs behave as nanoelectric dipoles. Therefore, nearby NPs in the SPR state can form bonding and antibonding states because they behave as nanodipoles. Nearby NPs in bonding states attract each other, and this is the driving effect to promote sintering.

Detailed MD simulations have been carried out to understand the coalescence process. Previous research[33] has highlighted the key role of the temperature in the different scenarios. When two Ag NPs are approaching and the touching interface is defect free and displays similar facets, an oriented attachment process[85] takes place, whereas when there is a plane mismatch at the interface between both Ag NPs, defects form along the IOA.[86,87]

The present work stresses the importance of long-time simulations to capture different events that occur at different times during the coalescence and sintering. Snapshots of the simulation, with a total time interval of Δt = 290 ns, are shown in Figure 3. Figure 3a shows snapshots of the coalescence process with two views. For each time label, two images are shown: on top, the atomic structure and at the bottom, the common neighbor analysis (CNA) cut that gives information about the internal structure of the Ag NP (green atoms are in an fcc structure, red atoms are in an hcp structure, and gray atoms are in a disordered structure). To help understand the overall evolution, some important distances are measured for the structures in Figure 3a and are presented in Figure 3b, namely, the length of the formed Ag NP (black line), the interface neck (green line), and the sizes of the two particles' radii (blue line for NP1 and red line for NP2). The evolution shows a clear decrease in the Ag NP size and a clear increase of the neck length, as it should be for the coalescence process; these results show reasonably well the same trends of the evolution seen in the experimental images. Figure 3a shows snapshots starting with the contact of the Ag NPs (t = 00 ns), as in the experiment, with a sharp edge formed by (111) surfaces of NP2 touching the (220) facet of NP1 at 40° (SI, Figure S5). Rotation of NP1 occurs in the early stages of attachment and evolves as the simulation progresses; this can be seen at t = 40 ns (SI, Figures S6 and S7). Therefore, orientation occurs to accommodate the contacting planes, but the touching surfaces are very different; thus, this process is a disorder-driven attachment event, for the short time span of Δt = 5 ns. Despite the rotation, the new Ag NP ends up with a disordered interface. While the rotation is understood from the Ag NP outer structure, as in the experiments, the CNA cut images help understand the type of interface produced (see the SI for Δt = 5 ns, Figure S8): it is a disordered interface, and some regions with defects are also formed, initially in NP2. The experiments show a rotation upon contact, and it is also observed in the early stages of the MD simulations. The merging occurs accompanied by the formation of a disordered interface, which lowers the surface energy and is maintained during the initial moments of the simulation (see Figure S8). It is important to note that this process is similar to the IOA mechanism observed by Penn and Banfield[86] and Li et al.,[87] in which NPs did not fully correct misalignment during attachment and the resulting interface consisted of grain boundary dislocations. It is well known that if the interface starts ordered, the total energy of the new structure is further lowered because defects are more energetic. At t = 60 ns, an unexpected ordering event occurred. The consequence of this event was a sudden lowering of the energy, as shown in Figure 3c, typical of phase transitions. In fact, a disorder-to-order transition was obtained. This striking event is shown in Figure 3a for t = 60 ns, and a detailed evolution of this effect in time steps of Δt = 10 ns is shown in Figure S9. Insets in the energy plot in Figure 3c and the detailed evolution in time steps of Δt = 0.1 ns in Figure 3d show details of the phase transition, in which the amorphous interface is pushed toward NP1. This conjunction of events, initially disorder-driven, forming a disordered interface that later evolves to an ordered interface because of the disorder-to-order transition, can be viewed as a two-stage ordering event. This effect could only be observed because of the extended simulation time considered in this study. This is important because, in the experiments, the time intervals between images are longer and this concerted behavior could be missed, with the ordered interface that resulted being considered as simple OA, which, due to the initial conditions, was not expected. Another effect of the ordering transition is that the occurrence of the new order enables the hcp stacking fault to evolve and permeate the whole extension of the Ag NP, producing, at the surface ends, disordered and mobile regions that can provide mobile atoms for surface diffusion as well as prevent the better faceting for which Wulff structures search (SI, Figure S9).

CONCLUSIONS

Exposure of Ag-containing materials to the EB unveiled new and interesting phenomena. Understanding the dynamics of NP formation and growth mechanisms is of great interest because the mode of assembling can influence the type of periodic lattice that is formed and, hence, the properties of the resulting nanocrystals. Watching the movements and dynamics of NPs and the subsequent assembling processes at high vacuum under the EB of a TEM provides helpful new insights. A complementary combination of atomistic MD simulations and in situ TEM images was utilized to increase the limited understanding of the sintering of Ag NPs, in the range from 4 to 8 nm, provoked by the EB irradiation on α-Ag_2WO_4 crystals in vacuum.

The conclusions of the present work are as follows. (i) The EB used to image the sample carries an electromagnetic field that produces SPR in the Ag NPs, forming neutral nanoelectric dipoles that are responsible for the corresponding coalescence processes. Then, the study provided a unique venue for the observation of the fundamental properties of SPR in confined electromagnetic fields, explained here as a dimer interaction between Ag NPs. (ii) MD simulations revealed that the coalescence process of the Ag NPs starts with a disorder-driven pathway or IOA mechanism followed by a structural disorder-to-order transition, via an OA mechanism. This also showed how healing and/or evolution of stacking faults contributes to

DOI: 10.1021/acs.jpcc.9b02107
J. Phys. Chem. C 2019, 123, 11310−11318

the formation of the Ag NP. (iii) The results presented shed new light on the various factors that dictate SPR-mediated coalescence processes in NPs and increase the understanding of plasmonic processes that can be triggered and/or controlled by the EBs. (iv) The mechanisms discussed herein make possible the synthesis of Ag NPs and, possibly, other structures in which the NPs are the building blocks that interact with the EB of the TEM. (v) The general methodology and insights gained from this in-depth study strengthen the understanding of sintering control for EB treatment because structural and energetic information is encoded in the evolution of Ag NPs.

■ ASSOCIATED CONTENT

Supporting Information

The Supporting Information is available free of charge on the ACS Publications website at DOI: 10.1021/acs.jpcc.9b02107.

MD simulations, production of simulated NPs, models for the Ag NPs at 500 K, temperature study of NP1 and NP2; sintering of simulated Ag NPs, additional analysis of simulated Ag NPs including nanoparticles NP1 and NP2 in the experiment and simulated Ag NPs, short-time evolution of the attachment process, details of rotation of NP2, CNA slice cut evolution, and structure and displacement of atoms during sintering (PDF)

Coalescence step (AVI)

■ AUTHOR INFORMATION

Corresponding Author

*E-mail: zacarias@ifi.unicamp.br.

ORCID

Edison Z. da Silva: 0000-0002-2195-0051

Thales R. Machado: 0000-0002-3246-6329

Nadia G. Macedo: 0000-0001-7031-2729

Marcelo de Assis: 0000-0003-0355-5565

Júlio C. Sczancoski: 0000-0002-8233-3268

Juan Andrés: 0000-0003-0232-3957

Elson Longo: 0000-0001-8062-7791

Author Contributions

The manuscript was done through the contributions of all authors. J.A., E.L., M.A.S.-M., and E.Z.d.S. conceived the project. E.L. conceived the idea of the experiment, while .E.Z.d.S., M.A.S.-M., and G.M.F. conceived the idea of molecular dynamics (MD) simulations. J.C.S. synthesized the initial Ag_2WO_4 precursor. T.R.M., N.G.M., M.d.A., and S.M.-J. performed the TEM experiments and collected the corresponding images and videos. G.M.F. performed the MD simulations. J.A., E.L., M.A.S.-M., E.Z.d.S., G.M.F., and T.R.M. discussed the results. G.M.F. drafted the manuscript. All authors read and approved the final manuscript.

Notes

The authors declare no competing financial interest.

■ ACKNOWLEDGMENTS

The authors thank the National Center for High Performance Computing in São Paulo (CENAPAD-SP), SDMONT at LLCC and the CCJDR-UNICAMP for providing the computational resources for this project. The following agencies contributed funds for this research: Coordenação de Aperfeiçoamento de pessoal de nível superior—Brasil (CAPES)—Finance code 001, PNPD Program, FINEP, FAPESP (2013/07296-2, 2016/23891-6), CNPq (150205/2017-1, EZDS, 304073/2015-6), UFGD, Generalitat Valenciana for Prometeo II/2014/022, ACOMP/2015/1202, Ministerio de Economia y Competitividad, project CTQ2015-65207-P, and Universitat Jaume I project No. UJI-B2016-25. The authors also thank Enio Longo for design contributions.

■ REFERENCES

(1) Gonzalez-Martinez, I. G.; Bachmatiuk, A.; Bezugly, V.; Kunstmann, J.; Gemming, T.; Liu, Z.; Cuniberti, G.; Rummeli, M. H. Electron-beam induced synthesis of nanostructures: a review. *Nanoscale* **2016**, *8*, 11340−11362.

(2) Liu, Y.; Lin, X.-M.; Sun, Y.; Rajh, T. *In situ* Visualization of Self-Assembly of Charged Gold Nanoparticles. *J. Am. Chem. Soc.* **2013**, *135*, 3764−3767.

(3) Huang, C.-W.; Chen, J.-Y.; Chiu, C.-H.; Hsin, C.-L.; Tseng, T.-Y.; Wu, W.-W. Observing the evolution of graphene layers at high current density. *Nano Res.* **2016**, *9*, 3663−3670.

(4) Liu, X.; Xu, T.; Wu, X.; Zhang, Z.; Yu, J.; Qiu, H.; Hong, J.-H.; Jin, C.-H.; Li, J.-X.; Wang, X.-R.; et al. Top-down fabrication of sub-nanometre semiconducting nanoribbons derived from molybdenum disulfide sheets. *Nat. Commun.* **2013**, *4*, No. 1776.

(5) Umalas, M.; Vlassov, S.; Polyakov, B.; Dorogin, L. M.; Saar, R.; Kink, I.; Lõhmus, R.; Lõhmus, A.; Romanov, A. E. Electron beam induced growth of silver nanowhiskers. *J. Cryst. Growth* **2015**, *410*, 63−68.

(6) Makita, Y.; Ikai, O.; Hosokawa, J.; Ooi, K.; Okuyama, S.; Sumida, N. Synthesis of Long Silver Nanowires by Electron Beam Irradiation on Ag-exchanged Material. *J. Ion Exch.* **2003**, *14*, 409−412.

(7) Edmondson, M. J.; Zhou, W.; Sieber, S. A.; Jones, I. P.; Gameson, I.; Anderson, P. A.; Edwards, P. P. Electron-Beam Induced Growth of Bare Silver Nanowires from Zeolite Crystallites. *Adv. Mater.* **2001**, *13*, 1608−1611.

(8) Yuan, Z.-Y.; Zhou, W.; Parvulescu, V.; Su, B.-L. Electron beam irradiation effect on nanostructured molecular sieve catalysts. *J. Electron Spectrosc. Relat. Phenom.* **2003**, *129*, 189−194.

(9) Li, K.; Zhang, F.-S. A novel approach for preparing silver nanoparticles under electron beam irradiation. *J. Nanopart. Res.* **2010**, *12*, 1423−1428.

(10) Makita, Y.; Osamu, I.; Akira, O.; Kenta, O. Preparation of Long Silver Nanowires from Silver Matrix by Electron Beam Irradiation. *Chem. Lett.* **2002**, *31*, 928−929.

(11) Ma, C.; Chen, X.; Tan, X.; Hu, P.; Li, Q.; Cao, Y.; Liang, X. In situ fabrication of silver-based nanostructures using electron beam. *CrystEngComm* **2018**, *20*, 2227−2232.

(12) Longo, E.; Cavalcante, L.; Volanti, D.; Gouveia, A. F.; Longo, V. M.; Varela, J. A.; Orlandi, M. O.; Andrés, J. Direct *in situ* observation of the electron-driven synthesis of Ag filaments on α-Ag_2WO_4 crystals. *Sci. Rep.* **2013**, *3*, No. 1676.

(13) Andrés, J.; Gracia, L.; Gonzalez-Navarrete, P.; Longo, V.; Avansi, W.; Volanti, D.; Ferrer, M.; Lemos, P.; La Porta, F.; Hernandes, A.; et al. Structural and electronic analysis of the atomic scale nucleation of Ag on α-Ag_2WO_4 induced by electron irradiation. *Sci. Rep.* **2014**, *4*, No. 5391.

(14) Longo, E.; Avansi, W.; Bettini, J.; Andrés, J.; Gracia, L. *In situ* Transmission Electron Microscopy observation of Ag nanocrystal evolution by surfactant free electron-driven synthesis. *Sci. Rep.* **2016**, *6*, No. 21498.

(15) San-Miguel, M. A.; da Silva, E. Z.; Zanetti, S. M.; Cilense, M.; Fabbro, M. T.; Gracia, L.; Andrés, J.; Longo, E. *In situ* growth of Ag nanoparticles on α-Ag_2WO_4 under electron irradiation: probing the physical principles. *Nanotechnology* **2016**, *27*, No. 225703.

(16) Roca, R. A.; Gouveia, A. F.; Lemos, P. S.; Gracia, L.; Andrés, J.; Longo, E. Formation of Ag Nanoparticles on β-Ag_2WO_4 through Electron Beam Irradiation: A Synergetic Computational and Experimental Study. *Inorg. Chem.* **2016**, *55*, 8661−8671.

(17) Roca, R. A.; Lemos, P. S.; Andrés, J.; Longo, E. Formation of Ag nanoparticles on metastable β-Ag_2WO_4 microcrystals induced by electron irradiation. *Chem. Phys. Lett.* **2016**, *644*, 68−72.

(18) Fabbro, M. T.; Saliby, C.; Rios, L. R.; Porta, F. A. L.; Gracia, L.; Li, M. S.; Andrés, J.; Santos, L. P. S.; Longo, E. Identifying and rationalizing the morphological, structural, and optical properties of α-Ag_2MoO_4 microcrystals, and the formation process of Ag nanoparticles on their surfaces: combining experimental data and first-principles calculations. *Sci. Technol. Adv. Mater.* **2015**, *16*, No. 065002.
(19) Fabbro, M. T.; Gracia, L.; Silva, G. S.; Santos, L. P.; Andrés, J.; Cordoncillo, E.; Longo, E. Understanding the formation and growth of Ag nanoparticles on silver chromate induced by electron irradiation in electron microscope: A combined experimental and theoretical study. *J. Solid State Chem.* **2016**, *239*, 220−227.
(20) de Oliveira, R. C.; Assis, M.; Teixeira, M. M.; da Silva, M. D. P.; Li, M. S.; Andrés, J.; Gracia, L.; Longo, E. An Experimental and Computational Study of β-Ag_2VO_3: Optical Properties and Formation of Ag Nanoparticles. *J. Phys. Chem. C* **2016**, *120*, 12254−12264.
(21) Botelho, G.; Sczancoski, J. C.; Andrés, J.; Gracia, L.; Longo, E. Experimental and Theoretical Study on the Structure, Optical Properties, and Growth of Metallic Silver Nanostructures in Ag_3PO_4. *J. Phys. Chem. C* **2015**, *119*, 6293−6306.
(22) Longo, V. M.; De Foggi, C. C.; Ferrer, M. M.; Gouveia, A. F.; André, R. S.; Avansi, W.; Vergani, C. E.; Machado, A. L.; Andrés, J.; Cavalcante, L. S.; et al. Potentiated Electron Transference in α-Ag_2WO_4 Microcrystals with Ag Nanofilaments as Microbial Agent. *J. Phys. Chem. A* **2014**, *118*, 5769−5778.
(23) Longo, E.; Volanti, D. P.; Longo, V. M.; Gracia, L.; Nogueira, I. C.; Almeida, M. A. P.; Pinheiro, A. N.; Ferrer, M. M.; Cavalcante, L. S.; Andrés, J. Toward an Understanding of the Growth of Ag Filaments on α-Ag_2WO_4 and Their Photoluminescent Properties: A Combined Experimental and Theoretical Study. *J. Phys. Chem. C* **2014**, *118*, 1229−1239.
(24) Liu, D.; Huang, W.; Li, L.; Liu, L.; Sun, X.; Liu, B.; Yang, B.; Guo, C. Experimental and theoretical investigation on photocatalytic activities of 1D Ag/Ag_2WO_4 nanostructures. *Nanotechnology* **2017**, *28*, No. 385702.
(25) Zhang, P.; Jiang, X.; Yuan, P.; Yan, H.; Yang, D. Silver nanopaste: Synthesis, reinforcements and application. *Int. J. Heat Mass Transfer* **2018**, *127*, 1048−1069.
(26) da Silva Pereira, W.; Andrés, J.; Gracia, L.; San-Miguel, M. A.; da Silva, E. Z.; Longo, E.; Longo, V. M. Elucidating the real-time Ag nanoparticle growth on α-Ag_2WO_4 during electron beam irradiation: experimental evidence and theoretical insights. *Phys. Chem. Chem. Phys.* **2015**, *17*, 5352−5359.
(27) Mansourian, A.; Paknejad, S. A.; Zayats, A. V.; Mannan, S. H. Stereoscopic Nanoscale-Precision Growth of Free-Standing Silver Nanorods by Electron Beam Irradiation. *J. Phys. Chem. C* **2016**, *120*, 20310−20314.
(28) Grouchko, M.; Roitman, P.; Zhu, X.; Popov, I.; Kamyshny, A.; Su, H.; Magdassi, S. Merging of metal nanoparticles driven by selective wettability of silver nanostructures. *Nat. Commun.* **2014**, *5*, No. 2994.
(29) Grammatikopoulos, P.; Cassidy, C.; Singh, V.; Sowwan, M. Coalescence-induced crystallisation wave in Pd nanoparticles. *Sci. Rep.* **2014**, *4*, No. 5779.
(30) José-Yacamán, M.; Gutierrez-Wing, C.; Miki, M.; Yang, D.-Q.; Piyakis, K. N.; Sacher, E. Surface Diffusion and Coalescence of Mobile Metal Nanoparticles. *J. Phys. Chem. B* **2005**, *109*, 9703−9711.
(31) Lange, A.; Samanta, A.; Majidi, H.; Mahajan, S.; Ging, J.; Olson, T.; van Benthem, K.; Elhadj, S. Dislocation mediated alignment during metal nanoparticle coalescence. *Acta Mater.* **2016**, *120*, 364−378.
(32) Pereira, Z. S.; da Silva, E. Z. Cold Welding of Gold and Silver Nanowires: A Molecular Dynamics Study. *J. Phys. Chem. C* **2011**, *115*, 22870−22876.
(33) Faccin, G. M.; San-Miguel, M. A.; Andrés, J.; Longo, E.; da Silva, E. Z. Computational Modeling for the Ag Nanoparticle Coalescence Process: A Case of Surface Plasmon Resonance. *J. Phys. Chem. C* **2017**, *121*, 7030−7036.
(34) Andrés, J.; Gouveia, A. F.; Gracia, L.; Longo, E.; Manzeppi Faccin, G.; da Silva, E. Z.; Pereira, D. H.; San-Miguel, M. A. Formation of Ag nanoparticles under electron beam irradiation: Atomistic origins from first-principles calculations. *Int. J. Quantum Chem.* **2018**, *118*, No. e25551.
(35) Li, M.; Hou, Q.; Wang, J. A molecular dynamics study of coalescence of tungsten nanoparticles. *Nucl. Instrum. Methods Phys. Res., Sect. B* **2017**, *410*, 171−178.
(36) Cheng, B.; Ngan, A. H. The crystal structures of sintered copper nanoparticles: A molecular dynamics study. *Int. J. Plast.* **2013**, *47*, 65−79.
(37) Gutiérrez-Wing, C.; Olmos-Asar, J.; Esparza, R.; Mariscal, M.; Yacamán, M. The role of ad-atoms in the coalescence of alkanethiol-passivated gold nanoparticles. *Electrochim. Acta* **2013**, *101*, 301−307.
(38) Hansen, T. W.; DeLaRiva, A. T.; Challa, S. R.; Datye, A. K. Sintering of Catalytic Nanoparticles: Particle Migration or Ostwald Ripening? *Acc. Chem. Res.* **2013**, *46*, 1720−1730.
(39) Li, Y.; Kalia, R. K.; Nakano, A.; Vashishta, P. Size effect on the oxidation of aluminum nanoparticle: Multimillion-atom reactive molecular dynamics simulations. *J. Appl. Phys.* **2013**, *114*, No. 134312.
(40) Xu, J.; Sakanoi, R.; Higuchi, Y.; Ozawa, N.; Sato, K.; Hashida, T.; Kubo, M. Molecular Dynamics Simulation of Ni Nanoparticles Sintering Process in Ni/YSZ Multi-Nanoparticle System. *J. Phys. Chem. C* **2013**, *117*, 9663−9672.
(41) Buesser, B.; Gröhn, A. J.; Pratsinis, S. E. Sintering Rate and Mechanism of TiO_2 Nanoparticles by Molecular Dynamics. *J. Phys. Chem. C* **2011**, *115*, 11030−11035.
(42) Zhao, H.; Gui, J.; Cao, J.; Zheng, C. Molecular Dynamics Simulation of the Microscopic Sintering Process of CuO Nanograins Inside an Oxygen Carrier Particle. *J. Phys. Chem. C* **2018**, *122*, 25595−25605.
(43) Stockman, M. I. Nanoplasmonics: past, present, and glimpse into future. *Opt. Express* **2011**, *19*, 22029−22106.
(44) Halas, N. J.; Lal, S.; Chang, W.-S.; Link, S.; Nordlander, P. Plasmons in Strongly Coupled Metallic Nanostructures. *Chem. Rev.* **2011**, *111*, 3913−3961.
(45) Szunerits, S.; Boukherroub, R. *Introduction to Plasmonics: Advances and Applications*; CRC Press: Boca Raton, FL, 2015.
(46) Powell, C. J.; Swan, J. B. Origin of the Characteristic Electron Energy Losses in Aluminum. *Phys. Rev.* **1959**, *115*, 869−875.
(47) Nelayah, J.; Kociak, M.; Stephan, O.; Garcia de Abajo, F. J.; Tence, M.; Henrard, L.; Taverna, D.; Pastoriza-Santos, I.; Liz-Marzan, L. M.; Colliex, C. Mapping surface plasmons on a single metallic nanoparticle. *Nat. Phys.* **2007**, *3*, 348−353.
(48) Liz-Marzán, L. M. Plasmonics. Electron Oscillations and Beyond. *J. Phys. Chem. Lett.* **2013**, *4*, 1197−1198.
(49) Alvarez-Puebla, R.; Liz-Marzán, L. M.; García de Abajo, F. J. Light Concentration at the Nanometer Scale. *J. Phys. Chem. Lett.* **2010**, *1*, 2428−2434.
(50) Xu, X.; Liu, G.; Azad, A. K. Visible light photocatalysis by *in situ* growth of plasmonic Ag nanoparticles upon $AgTaO_3$. *Int. J. Hydrogen Energy* **2015**, *40*, 3672−3678.
(51) Lu, Y.; Shen, Q.; Yu, Q.; Zhang, F.; Li, G.; Zhang, W. Photoinduced *in situ* Growth of Ag Nanoparticles on $AgNbO_3$. *J. Phys. Chem. C* **2016**, *120*, 28712−28716.
(52) Brus, L. Plasmon-driven chemical synthesis: Growing gold nanoprisms with light. *Nat. Mater.* **2016**, *15*, 824−825.
(53) Zhai, Y.; DuChene, J. S.; Wang, Y.-C.; Qiu, J.; Johnston-Peck, A. C.; You, B.; Guo, W.; DiCiaccio, B.; Qian, K.; Zhao, E. W.; et al. Polyvinylpyrrolidone-induced anisotropic growth of gold nanoprisms in plasmon-driven synthesis. *Nat. Mater.* **2016**, *15*, 889−895.
(54) Koh, A. L.; Bao, K.; Khan, I.; Smith, W. E.; Kothleitner, G.; Nordlander, P.; Maier, S. A.; McComb, D. W. Electron Energy-Loss Spectroscopy (EELS) of Surface Plasmons in Single Silver Nanoparticles and Dimers: Influence of Beam Damage and Mapping of Dark Modes. *ACS Nano* **2009**, *3*, 3015−3022.
(55) Prodan, E.; Radloff, C.; Halas, N. J.; Nordlander, P. A Hybridization Model for the Plasmon Response of Complex Nanostructures. *Science* **2003**, *302*, 419−422.
(56) Prodan, E.; Nordlander, P. Plasmon hybridization in spherical nanoparticles. *J. Chem. Phys.* **2004**, *120*, 5444−5454.

DOI: 10.1021/acs.jpcc.9b02107
J. Phys. Chem. C 2019, 123, 11310−11318

(57) Sczancoski, J. C.; Maya-Johson, S.; da Silva Pereira, W.; Longo, E.; Leite, E. R. Atomic Diffusion Induced by Electron-Beam Irradiation: An in Situ Study of Ag Structures Grown from α-Ag_2WO_4. *Cryst. Growth Des.* **2019**, 106−115.
(58) Plimpton, S. Fast Parallel Algorithms for Short-Range Molecular Dynamics. *J. Comput. Phys.* **1995**, *117*, 1−19.
(59) Brown, W. M.; Wang, P.; Plimpton, S. J.; Tharrington, A. N. Implementing molecular dynamics on hybrid high performance computers - short range forces. *Comput. Phys. Commun.* **2011**, *182*, 898−911.
(60) Brown, W. M.; Kohlmeyer, A.; Plimpton, S. J.; Tharrington, A. N. Implementing molecular dynamics on hybrid high performance computers - Particle-particle particle-mesh. *Comput. Phys. Commun.* **2012**, *183*, 449−459.
(61) Brown, W. M.; Yamada, M. Implementing molecular dynamics on hybrid high performance computers-Three-body potentials. *Comput. Phys. Commun.* **2013**, *184*, 2785−2793.
(62) Daw, M. S.; Baskes, M. I. Embedded-atom method: Derivation and application to impurities, surfaces, and other defects in metals. *Phys. Rev. B* **1984**, *29*, 6443−6453.
(63) Foiles, S. M.; Baskes, M. I.; Daw, M. S. Embedded-atom-method functions for the fcc metals Cu, Ag, Au, Ni, Pd, Pt, and their alloys. *Phys. Rev. B* **1986**, *33*, 7983−7991.
(64) Johnson, R. A. Alloy models with the embedded-atom method. *Phys. Rev. B* **1989**, *39*, 12554−12559.
(65) Mishin, Y.; Farkas, D.; Mehl, M. J.; Papaconstantopoulos, D. A. Interatomic potentials for monoatomic metals from experimental data and ab initio calculations. *Phys. Rev. B* **1999**, *59*, 3393−3407.
(66) Sheng, H. W.; Kramer, M. J.; Cadien, A.; Fujita, T.; Chen, M. W. Highly optimized embedded-atom-method potentials for fourteen fcc metals. *Phys. Rev. B* **2011**, *83*, No. 134118.
(67) Sun, J.; He, L.; Lo, Y.-C.; Xu, T.; Bi, H.; Sun, L.; Zhang, Z.; Mao, S. X.; Li, J. Liquid-like pseudoelasticity of sub-10-nm crystalline silver particles. *Nat. Mater.* **2014**, *13*, 1007−1012.
(68) Filleter, T.; Ryu, S.; Kang, K.; Yin, J.; Bernal, R. A.; Sohn, K.; Li, S.; Huang, J.; Cai, W.; Espinosa, H. D. Nucleation-Controlled Distributed Plasticity in Penta-twinned Silver Nanowires. *Small* **2012**, *8*, 2986−2993.
(69) Sun, G.; Xu, J.; Harrowell, P. The mechanism of the ultrafast crystal growth of pure metals from their melts. *Nat. Mater.* **2018**, 1476−4660.
(70) Huang, W. J.; Sun, R.; Tao, J.; Menard, L. D.; Nuzzo, R. G.; Zuo, J. M. Coordination-dependent surface atomic contraction in nanocrystals revealed by coherent diffraction. *Nat. Mater.* **2008**, *7*, 308.
(71) Nosé, S. A molecular dynamics method for simulations in the canonical ensemble. *Mol. Phys.* **1984**, *52*, 255−268.
(72) Nosé, S. A unified formulation of the constant temperature molecular dynamics methods. *J. Chem. Phys.* **1984**, *81*, 511−519.
(73) Hoover, W. G. Canonical dynamics: Equilibrium phase-space distributions. *Phys. Rev. A* **1985**, *31*, 1695−1697.
(74) Humphrey, W.; Dalke, A.; Schulten, K. VMD: Visual molecular dynamics. *J. Mol. Graphics* **1996**, *14*, 33−38.
(75) Varshney, A.; Brooks, F. P.; Wright, W. V. Computing smooth molecular surfaces. *IEEE Comput. Graphics Appl.* **1994**, *14*, 19−25.
(76) Stukowski, A. Visualization and analysis of atomistic simulation data with OVITO-the Open Visualization Tool. *Modell. Simul. Mater. Sci. Eng.* **2010**, *18*, No. 015012.
(77) Honeycutt, J. D.; Andersen, H. C. Molecular dynamics study of melting and freezing of small Lennard-Jones clusters. *J. Phys. Chem.* **1987**, *91*, 4950−4963.
(78) Li, J.; Chen, J.; Wang, H.; Chen, N.; Wang, Z.; Guo, L.; Deepak, F. L. In Situ Atomic-Scale Study of Particle-Mediated Nucleation and Growth in Amorphous Bismuth to Nanocrystal Phase Transformation. *Adv. Sci.* **2018**, *5*, No. 1700992.
(79) Pyrz, W. D.; Park, S.; Vogt, T.; Buttrey, D. J. Electron Beam-Induced Fragmentation and Dispersion of Bi-Ni Nanoparticles. *J. Phys. Chem. C* **2007**, *111*, 10824−10828.
(80) Assis, M.; Macedo, N. G.; Machado, T. R.; Ferrer, M. M.; Gouveia, A. F.; Cordoncillo, E.; Torres-Mendieta, R.; Beltrán-Mir, H.; Mínguez-Vega, G.; Leite, E. R.; et al. Laser/Electron Irradiation on Indium Phosphide (InP) Semiconductor: Promising Pathways to In Situ Formation of Indium Nanoparticles. *Part. Part. Syst. Charact.* **2018**, *35*, No. 1800237.
(81) Hill, T. L. *Statistical Mechanics*; McGraw-Hill, 1956.
(82) Sinanoglu, O. *Modern Quantum Chemistry*; Academic Press, 1965.
(83) Aabdin, Z.; Lu, J.; Zhu, X.; Anand, U.; Loh, N. D.; Su, H.; Mirsaidov, U. Bonding Pathways of Gold Nanocrystals in Solution. *Nano Lett.* **2014**, *14*, 6639−6643.
(84) Nordlander, P.; Oubre, C.; Prodan, E.; Li, K.; Stockman, M. I. Plasmon Hybridization in Nanoparticle Dimers. *Nano Lett.* **2004**, *4*, 899−903.
(85) Wang, Y. Q.; Liang, W. S.; Geng, C. Y. Coalescence Behavior of Gold Nanoparticles. *Nanoscale Res. Lett.* **2009**, *4*, 684.
(86) Penn, R. L.; Banfield, J. F. Imperfect Oriented Attachment: Dislocation Generation in Defect-Free Nanocrystals. *Science* **1998**, *281*, 969−971.
(87) Li, D.; Nielsen, M. H.; Lee, J. R. I.; Frandsen, C.; Banfield, J. F.; De Yoreo, J. J. Direction-Specific Interactions Control Crystal Growth by Oriented Attachment. *Science* **2012**, *336*, 1014−1018.

DOI: 10.1021/acs.jpcc.9b02107
J. Phys. Chem. C 2019, 123, 11310−11318